Int J Adv Manuf Technol (2017) 91:2681–2688
DOI 10.1007/s00170-016-9917-1

ORIGINAL ARTICLE

Comparative study of hybrid laser–MIG leading configuration on porosity in aluminum alloy bead-on-plate welding

Haibin Miao [1,2] · Gang Yu [1,2] · Xiuli He [1,2] · Shaoxia Li [1,2] · Xuyang Chen [1,2]

Received: 26 August 2016 / Accepted: 18 December 2016 / Published online: 9 January 2017

Abstract Laser–metal inert gas (MIG) welding is a promising welding technology, which presents many attractive properties. However, porosity still remains a serious problem in laser–MIG welding of aluminum. In this experimental study, the effect of leading configuration on porosity formation and distribution in laser–MIG bead-on-plate welding of A7N01 alloy was investigated. Experiments on arc current, welding speed, and arc configuration were performed comparatively for two leading configurations, respectively. The welds were analyzed with X-ray photographs and cross-section observations. Pores in laser–MIG-welded samples were mainly keyhole-induced. The concept of porosity area fraction was used to evaluate the severity of pore defect. The maximum porosity area fraction presented at different arc currents in the two leading configurations (in laser leading welding, it is 150 A, while in arc leading welding, it is 110 A). With welding speed increasing, porosity area fraction decreased. Bubble escape condition was deduced and used to discuss the probable mechanism of the effect of leading configuration on pore formation. The results showed that leading configuration was considerable in porosity minimization and prevention.

Keywords Laser–MIG hybrid welding · A7N01 aluminum alloy · Leading configuration · Porosity

✉ Gang Yu
gyu@imech.ac.cn

1 Key Laboratory of Mechanics in Advanced Manufacturing, Institute of Mechanics, Chinese Academy of Sciences, Beijing 100190, China

2 School of Engineering Science, University of Chinese Academy of Sciences, Beijing 100049, China

1 Introduction

A7N01 is a heat-treatable aluminum alloy which is widely used in high-speed vehicle body. The components of the body are mainly jointed by welding. Laser–metal inert gas (MIG) welding, which was originally proposed by Steen WM [1], combined the techniques of laser welding and arc welding. It has very attractive properties: higher welding speeds, thicker welded materials, joint fit-up allowance, better stability of molten pool, and improvement of metallurgical quality [2]. Application of laser–MIG welding of A7N01 alloy in high-speed vehicle industry is promising.

However, porosity still remains a serious problem in laser–MIG welding of aluminum, as it deteriorates mechanical properties, particularly tensile strength and elongation [3]. The influence of various parameters on porosity formation and distribution in laser–MIG welding of aluminum alloys has been reported. The effect of laser power, arc current, welding speed, standoff distance, and defocus amount was investigated by many researches [4–10]. Leo et al. also studied the effect of power distribution on the weld quality including porosity defect evaluation during hybrid laser welding of an Al–Mg alloy [11]. The leading configuration, which indicates the relative location of laser and arc, has a great influence on penetration and fluid flow [12, 13]. It also should have an effect on porosity formation and distribution. However, few researches focused on this study. Cross sections were observed in [14] to investigate the influence of leading configuration on porosity. Porosity defects of two leading configurations under different off-distances were detected with X-ray technique in [15]. However, in different leading configurations, various parameters such as arc currents, welding speeds, and arc configurations were not investigated. Therefore, for the purpose of porosity minimization and prevention, various parameters in two leading configurations should be considered and investigated.

Table 1 Compositions of the base alloy and the welding wire

Materials	Mg	Zn	Si	Fe	Mn	Cr	Ti	Zr	Cu	Al
A7N01	1.0–2.0	4.0–5.0	<0.30	0.35	0.2–0.7	<0.30	<0.20	<0.25	<0.2	Bal.
ER5356	4.5–5.5	<0.1	<0.25	<0.4	0.05–0.2	0.05–0.2	0.06–0.2	–	<0.1	Bal.

Accordingly, in this study, experimental investigation of different arc currents, welding speeds, and arc configurations was performed comparatively for two leading configurations, respectively. X-ray photographs were taken to reveal the distribution of internal pores in laser–MIG bead-on-plate welding of aluminum alloy. The concept of porosity area fraction was adopted to evaluate the severity of pore defect. Also, mathematical expression of bubble escape condition was deduced and used to illustrate the porosity formation process.

2 Materials and experimental procedures

The specimens were made of commercial aluminum A7N01 (Al–Zn–Mg alloy) with the geometry of 6-mm × 100-mm × 200-mm sheet. The alloy was in the T5 condition. The MIG wire was ER5356 of 1.2 mm in diameter. The compositions of the base alloy and the welding wire are presented in Table 1.

The laser with the maximum power of 1 kW and continuous wavelength of 1070 nm was delivered through a fiber of 150 μm in diameter. The laser head consisted of a collimating lens of 150 mm and focusing lens of 300 mm. A pulsed MIG welding machine (maximum current 350 A) was employed as arc power source.

Arc configuration is different according to different welding directions: “push” and “pull” (Fig. 1a). Arc configuration has a great influence on weld pool shape and fluid flow [13]. The MIG torch was tilted to laser head with an angle. In laser leading configuration, the arc was “push” configuration, while in arc leading configuration, the arc was “pull” configuration (Fig. 1b). Corresponding MIG experiments were performed in order to understand the effect of arc configuration. Bead-on-plate welding on leading configuration was comparatively carried out by varying arc currents, welding speeds, and arc configurations, respectively. The welding process parameters are shown in Table 2

In order to analyze porosity in the weldments, X-ray photographs were carried out in the direction perpendicular to the sample surface. ISO 10042:2005 and ISO 13919-2:2001 were referred to define porosity area fraction (described in Fig. 2 and Eq. (1)). The concept was used to evaluate the severity of pores. A rectangular area was defined to include all the pores exactly, and the relative porosity area percentage was calculated as porosity area fraction. Also, the welded samples were sectioned transverse to the welding direction for microstructural analysis.

$$\mathbf{f} = \mathbf{S}_p \Big/ S_t \tag{1}$$

where f is the porosity area fraction, S_p is the total area of pores, and S_t is the total area of the rectangle.

The weld appearance was observed with SEM, and the chemical compositions of surface covering were analyzed with EDS. The morphology of pores was observed with optical microscope.

3 Results and discussion

3.1 Bubble generation and its escape process

Laser–MIG welding is a keyhole mode welding. Keyhole-induced pores [16–18] widely exist in hybrid weld. The molten metal on the rear wall moves in to fill the space vacated by the front wall of the keyhole. If the keyhole wall is unstable, the metal may fail to fill the cavity smoothly. As a result, the

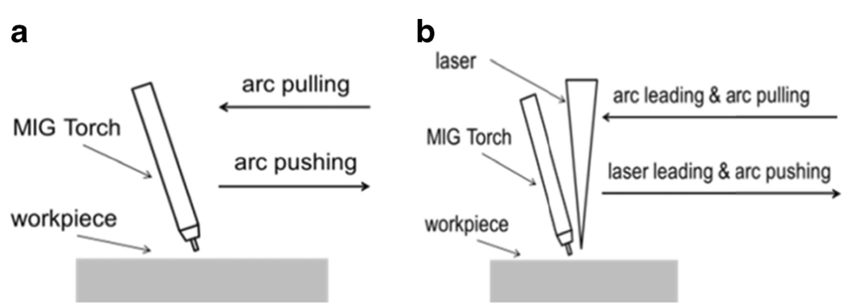

Fig. 1 Schematic of leading configurations and arc configurations. **a** Arc configurations. **b** Leading configurations

Table 2 Process parameters

Laser	
Power (W)	0, 850
Defocused amount	−2 mm
MIG	
Current (A)	70, 110, 150, 190
Torch angle	22°
Wire	ER5356/φ1.2 mm
Arc configuration	Push, pull
Shielding gas	99.99% Ar, 15 L/min
Off-distance	2 mm
Welding speed (mm/s)	10, 12, 18, 26
Leading configuration	Laser leading, arc leading

metal vapor and gases are entrapped at the root of the weld [19]. The balance of pressures in the keyhole can be expressed as follows [20–23]:

$$P_r + P_h = P_{abl} + \delta P_g \tag{2}$$

where P_r and P_h are surface tension pressure and hydrostatic pressure, respectively, which tend to close the keyhole. P_{abl} is recoil pressure and δP_g is excess vapor pressure, which tend to open the keyhole.

The interruption of the balance of pressures would lead to the collapse of keyhole. Bubbles intermittently generate at the bottom of the keyhole. During the bubble escape process, if bubbles are captured by solidifying front, pores would be formed. Therefore, the bubble escape process is discussed below.

In laser–MIG welding of aluminum, most of the pores are keyhole-induced [24–26]. Bubbles move in the liquid pool. Some of the bubbles escape to the atmosphere, and others are captured by solidifying front, which is the basic porosity formation process. The process was mentioned by many researches from the point of bubble-rising time and molten pool solidification time [27–30]. However, molten pool shape, bubble velocity, and velocity of solidifying front should be considered at the same time. The process from bubble movement to escaping or being captured by solidifying front is schematically described in Fig. 3.

Bubble velocity is decomposed into an x and a y direction, indicated by u and w, respectively. Suppose a bubble is

Fig. 2 Extraction of porosity profile and rectangular defined area

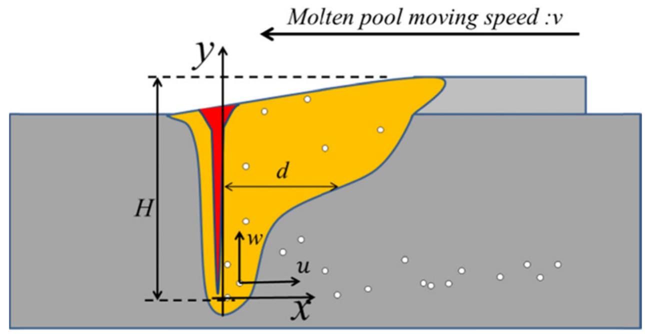

Fig. 3 Schematic description of bubble movement process

generated from the keyhole tip, the time needed to escape from the liquid molten pool can be expressed as follows:

$$H = \int_0^{t_0} w \, \mathrm{dt} \tag{3}$$

where H is the distance from the location of bubble formation to pool surface and t_0 is the time needed to escape from the liquid molten pool.

Moreover, during this period, the bubble should not be captured by solidifying front; thus, the following conditions must be met:

$$\begin{aligned} &\text{for any } t' \in (0, t_0) \\ &\int_0^{t'} u dt + vt \le d \end{aligned} \tag{4}$$

where v is the moving speed of the molten pool and d is the distance between solidifying front and keyhole wall.

Also, d was the function of y:

$$d = d(y) \tag{5}$$

while

$$y = \int_0^{t'} w dt \tag{6}$$

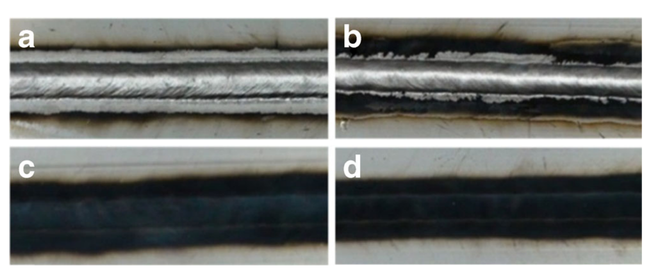

Fig. 4 Weld appearances under different configurations. **a** Laser leading. **b** Push. **c** Arc leading. **d** Pull

Fig. 5 Dark gray covering image of SEM and EDS analysis results

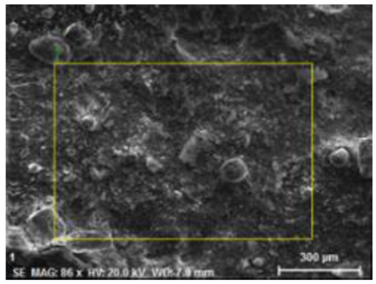

El	Atom.C(%)	Error(%)
O	54.8	7.3
Al	25.2	1.1
Mg	20.0	0.9

So, bubble escape condition can be summarized as follows:

$$\text{for any} \quad t' \in (0, t_0) \quad \int_0^{t'} u\,dt + vt \le d(y),\ y = \int_0^{t'} w\,dt \tag{7}$$

In conclusion, bubble escape process is affected by weld pool shape, welding speed, and bubble velocity. Any parameters that affect those factors mentioned above will have an effect on porosity formation.

3.2 Weld appearance

Figure 4 shows the weld bead appearances under different welding configurations. In laser leading and arc pushing

Table 3 X-ray inspection and cross-section observation results on arc currents in different configurations

Current (A)	Laser leading	Push ($P°=°0°W$)	Arc leading	Pull ($P°=°0°W$)
70	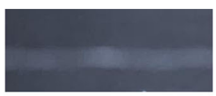			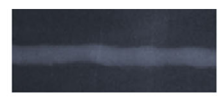
		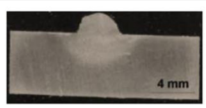	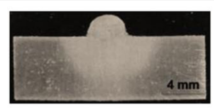	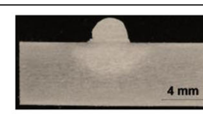
110				
	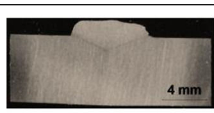	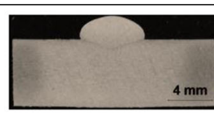	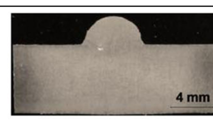	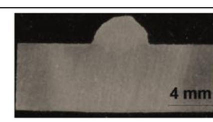
150				
	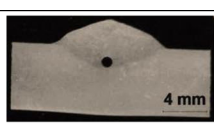	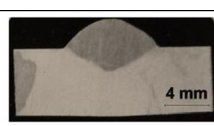	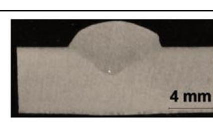	
190		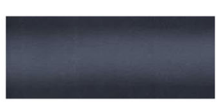		
	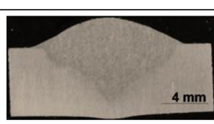			

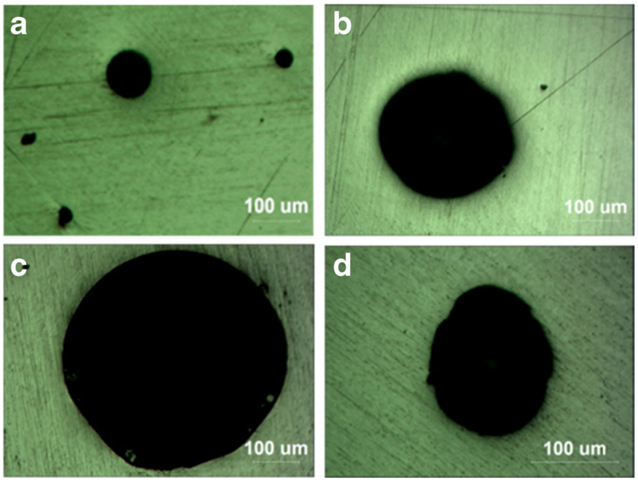

Fig. 6 Optical image of macro- and micropores in different leading configurations. **a** Laser leading and I = 110 A. **b** Arc leading and I = 110 A. **c** Laser leading and I = 150 A. **d** Arc leading and I = 150A

configurations, bright and clean surface was achieved. By contrast, a dark gray appearance was exhibited in arc leading and arc pulling configurations. To ascertain the constituent of the dark gray covering, EDS and SEM analyses were made. According to the results shown in Fig. 5, the chemical compositions of it are mainly Al, Mg, and O. Therefore, the dark gray appearance was caused by Al–Mg–O oxide particles that adhered to the bead surface. Moreover, cathode cleaning area in laser leading welding was more tidy and wider than that in arc pushing.

3.3 The effect of laser on pore formation

The X-ray inspection and cross-section observation results on arc currents in different configurations are shown in Table 3. Porosity was found in both laser leading and arc leading hybrid welding but was absent in arc welding. Most of the pores lied around the middle of beads in hybrid weld. The introduction of laser increased the incidence of porosity, and the detected pores were keyhole-induced.

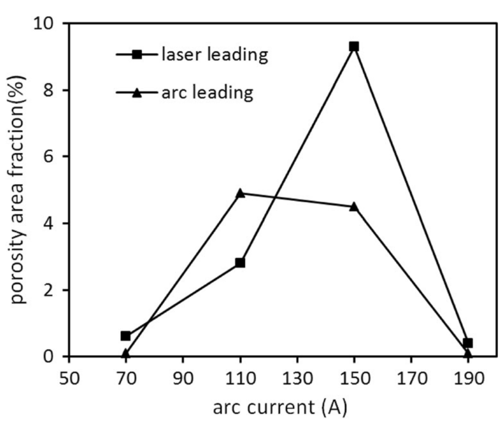

Fig. 7 Porosity area fractions under different arc currents and leading configurations

Morphology of pores is shown in Fig. 6. Pore size under I = 150 A was relatively bigger than that under I = 110 A. Irregular-shaped pores like ellipse were also observed, which may be ascribed to irregular keyhole closure or shrinking. According to Table 3, macropores were mostly distributed along the edges and at the root of the weld bead. It can be explained by the fact that those locations solidified first, and bubbles brought by convection flow were easily captured by solidification front.

3.4 Pore distribution under arc currents in different leading configurations

The X-ray inspection and cross-section observation results on arc currents in different configurations are shown in Table 3. Porosity area fractions under different arc currents and leading configurations are reported in Fig. 7. With arc current increasing, porosity area fraction increased at first and then decreased. For laser leading welding, the maximum porosity area fraction is about 9% when the arc current is 150 A; for arc leading welding, the maximum is about 5% when the arc current is 110 A.

At I = 70 A, it can be explained by the fact that the penetration was too shallow and bubbles can hardly be captured by solidifying front. When the arc current was high enough, the welds were nearly porosity-free, which was also observed by some other researchers [7, 10]. The mechanism was believed to be that the molten pool was strongly pushed down by arc pressure and a concave surface produced. In this way, bubbles generated from keyhole disappeared into the atmosphere easier through the molten pool surface suppressed by arc pressure.

3.5 Pore distribution under welding speeds in different leading configurations

X-ray inspection and cross-section observation results on welding speeds in different configurations are shown in Table 4. Pores lied mostly around the middle of beads in laser–MIG weld. Average pore size in laser leading welding was bigger than that in arc leading welding, but with the increase of welding speed, pore size difference was not obvious.

Porosity area fractions under different welding speeds and leading configurations are shown in Fig. 8. With welding speed increasing, porosity area fraction decreased. In fact, pore size was also decreased. The reason was that high welding speed made a smaller keyhole and a shallower penetration. In this way, bubble size was smaller and could escape easier.

Table 4 X-ray inspection and cross-section observation results on welding speeds in different configurations

Speed (mm/s)	Laser leading	Push ($P°=°0°W$)	Arc leading	Pull ($P°=°0°W$)
10				
	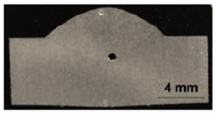	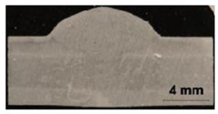	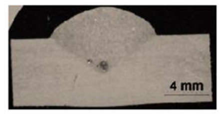	
18				
		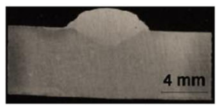	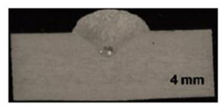	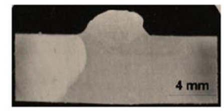
26				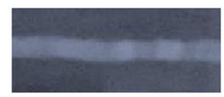
			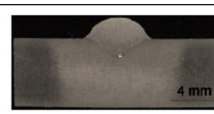	

3.6 Discussion of the effect of leading configuration on pore formation

Equation (7) showed that bubble escape process was affected by weld pool shape, welding speed, and bubble velocity. Figure 9 presents the schematic description of weld pool shape in different leading configurations.

The molten pool was divided into "arc zone" and "laser zone" [31, 32], which referred to typical weld pool shape of arc welding and laser welding, respectively. According to Fig. 9, the arc zone is wider and the laser zone is deeper in laser leading welding than in arc leading welding. Therefore, in arc leading welding, bubbles escape easier from the "laser zone" to "arc zone" but it is harder to continue escaping in the arc zone. In laser leading welding, the opposite is the case. X-ray inspection results showed that pores were more decentralized from the middle of welds in arc leading welding. The reason was that in arc leading welding, more bubbles were captured in the arc zone, resulting in a more decentralized distribution.

The height of molten pool can be indicated by penetration plus reinforcement. According to Fig. 10a, with arc current increasing, the height of molten pool in arc leading welding was much higher at $I = 110$ A. Thus, a longer escape distance

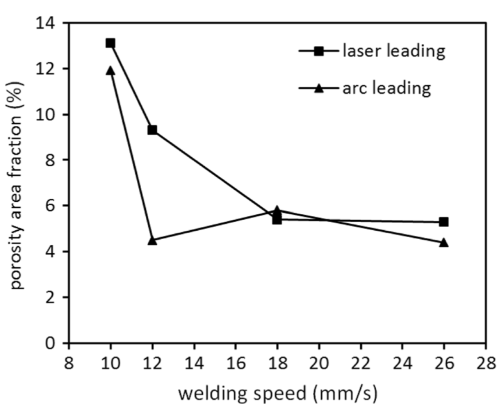

Fig. 8 Porosity area fractions under different welding speeds and leading configurations

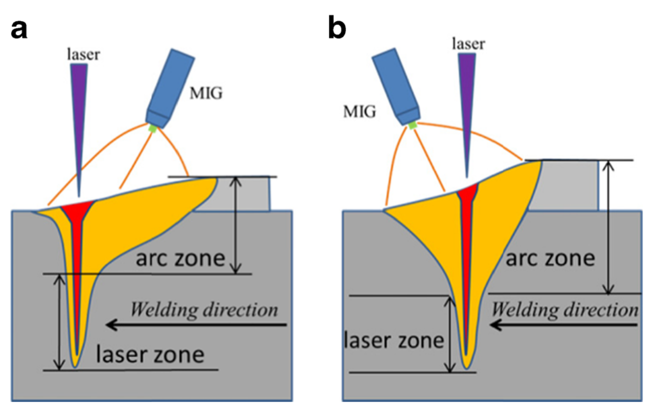

Fig. 9 Schematic description of weld shape in different leading configurations. **a** Laser leading. **b** Arc leading

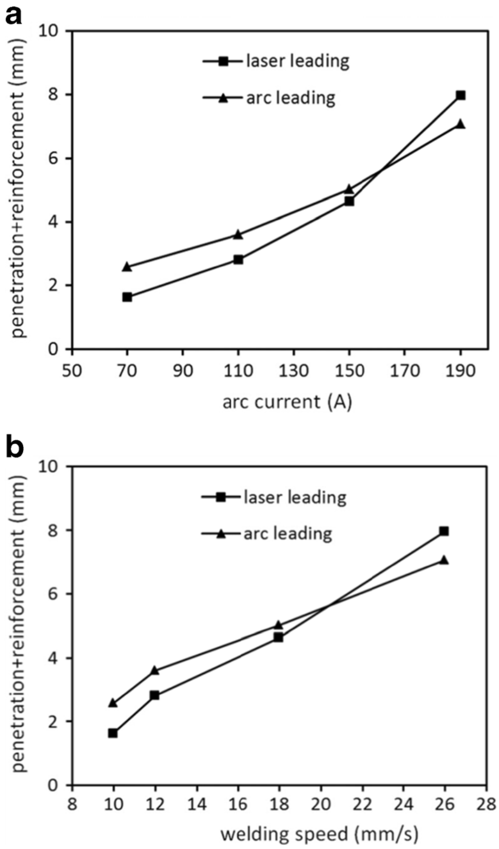

Fig. 10 Penetration + reinforcement of different leading configurations. **a** Under various arc currents. **b** Under various welding speeds

H was needed and the bubbles were easier to be captured by solidifying front. At $I = 150$ A, when the height of molten pool was nearly the same, for arc leading welding, a much less porosity area fraction was presented. The reason was considered to be that, in arc leading welding, bubbles generated at the keyhole tip could enter the arc zone easier and subsequently easily escaped.

According to Fig. 10b, with welding speed increasing, the height of molten pool decreased. As a result, a shorter escape distance H was need and bubbles escaped easily, so porosity area fraction decreased. At $v = 12$ mm/s, porosity area fraction was much lower in arc leading than in laser leading welding. The probable reason was that, arc leading welding achieved appropriate combination of weld pool shape and flow regime.

In all, weld pool shape, welding speed, and bubble velocity were the key to decreasing porosity. From this point of view, leading configuration should also be considered in porosity minimization and prevention.

4 Conclusions

The size, shape, and distribution of pores were comparatively investigated under laser leading welding and arc leading welding in laser–MIG bead-on-plate welding of aluminum alloy. The conclusions could be summarized as follows:

1. Bubble escape condition was deduced to elucidate porosity formation mechanism. It was pointed out with mathematical expression that bubble escape process was influenced by weld pool shape, welding speed, and bubble velocity.
2. When the arc current was 110–150 A, keyhole-induced porosity was found in both laser leading welding and arc leading hybrid welding, but absent in arc welding. Therefore, the introduction of laser increased the incidence of porosity.
3. With welding speed increasing, porosity area fraction decreased from 13 to 5% and 12 to 4% respectively for laser leading welding and arc leading welding. Pore size was also decreased.
4. With arc current increasing, porosity area fraction increased at first and then decreased. The maximum porosity area fraction presented at different arc currents for the two leading configurations (for laser leading welding, it is 150 A with 9%, while for arc leading welding, it is 110 A with 5%).
5. For arc leading welding, bubbles generated at the keyhole tip could enter the arc zone easier while more difficult to continue escaping in the arc zone. In laser leading welding, the opposite is the case.

In summary, an appropriate combination of weld pool shape, welding speed, and bubble velocity should be made to decrease porosity. Leading configuration should be necessarily considered in porosity minimization and prevention.

Acknowledgments The authors are grateful for the support of the National Natural Science Foundation of China under grant no.11272316, 11272317, and 11502269.

References

1. Steen WM, Eboo M (1979) Arc augmented laser-welding. Met Constr-Brit Weld 11(7):332–336
2. Le Guen E, Fabbro R, Carin M, Coste F, Le Masson P (2011) Analysis of hybrid Nd:Yag laser-MAG arc welding processes. Optics & Laser Technology 43(7):1155–1166. doi:10.1016/j.optlastec.2011.03.002
3. Wang J, Wang GZ, Wang CM (2015) Mechanisms of the porosity formation during the fiber laser lap welding of aluminium alloy. Metalurgija 54(4):683–686
4. Casalino G, Mortello M, Leo P, Benyounis KY, Olabi AG (2014) Study on arc and laser powers in the hybrid welding of AA5754 Al-alloy. Mater Design 61:191–198. doi:10.1016/j.matdes.2014.04.060
5. Ola OT, Doern FE (2015) Keyhole-induced porosity in laser-arc hybrid welded aluminum. Int J Adv Manuf Tech 80(1–4):3–10. doi:10.1007/s00170-015-6987-4

6. Campana G, Ascari A, Fortunato A, Tani G (2009) Hybrid laser-MIG welding of aluminum alloys: the influence of shielding gases. Appl Surf Sci 255(10):5588–5590. doi:10.1016/j.apsusc.2008.07.169
7. Katayama S, Uchiumi S, Mizutani M, Wang J, Fujii K (2007) Penetration and porosity prevention mechanism in YAG laser-MIG hybrid welding. Weld Int 21(1):25–31. doi:10.1533/wint.2007.3680
8. Wang QY, Chen H, Zhu ZT, Qiu PX, Cui YL (2016) A characterization of microstructure and mechanical properties of A6N01S-T5 aluminum alloy hybrid fiber laser-MIG welded joint. Int J Adv Manuf Tech 86(5–8):1375–1384
9. Liu S, Li JM, Mi GY, Wang CM, Hu XY (2016) Study on laser-MIG hybrid welding characteristics of A7N01-T6 aluminum alloy. Int J Adv Manuf Tech 87(1–4):1135–1144
10. Katayama S, Uchiumi S, Briand F (2006) Production of sound deep-penetration hybrid weld in aluminum alloy with YAG laser and MIG arc. Proceedings of the 22nd ICALEO, 953–959
11. Leo P, Renna G, Casalino G, Olabi AG (2015) Effect of power distribution on the weld quality during hybrid laser welding of an Al-Mg alloy. Opt Laser Technol 73:118–126
12. Kah P, Salminen A, Martikainen J (2010) The effect of the relative location of laser beam with arc in different hybrid welding processes. Mechanika 3:68–74
13. Zhao L, Sugino T, Arakane G, Tsukamoto S (2009) Influence of welding parameters on distribution of wire feeding elements in CO2 laser GMA hybrid welding. Sci Technol Weld Joi 14(5):457–467. doi:10.1179/136217109x434252
14. Casalino G, Campanelli SL, Dal Maso U, Ludovico AD (2013) Arc leading versus laser leading in the hybrid welding of aluminium alloy using a fiber laser. Procedia CIRP 12:151–156. doi:10.1016/j.procir.2013.09.027
15. Katayama S, Mizutani M (2003) Elucidation of laser welding phenomena and porosity formation mechanism (physics, processes, instruments & measurements, international symposium of JWRI 30th anniversary). Trans JWRI 32:67–69
16. Haboudou A, Peyre P, Vannes AB (2004) Influence of surface preparation and process parameters on the porosity generation in aluminum alloys. J Laser Appl 16(1):20–24. doi:10.2351/1.1619995
17. AlShaer AW, Li L, Mistry A (2014) The effects of short pulse laser surface cleaning on porosity formation and reduction in laser welding of aluminium alloy for automotive component manufacture. Opt Laser Technol 64:162–171. doi:10.1016/j.optlastec.2014.05.010
18. Yao W, Gong SL (2011) Porosity formation mechanisms and controlling technique for laser penetration welding. Adv Mater Res-Switz 287-290:2191–2194. doi:10.4028/www.scientific.net/AMR.287-290.2191
19. Zhao H, White DR, DebRoy T (1999) Current issues and problems in laser welding of automotive aluminium alloys. Int Mater Rev 44(6):238–266. doi:10.1179/095066099101528298
20. Pang SY, Chen X, Zhou JX, Shao XY, Wang CM (2015) 3D transient multiphase model for keyhole, vapor plume, and weld pool dynamics in laser welding including the ambient pressure effect. Opt Laser Eng 74:47–58. doi:10.1016/j.optlaseng.2015.05.003
21. You DY, Gao XD, Katayama S (2015) Detection of imperfection formation in disk laser welding using multiple on-line measurements. J Mater Process Tech 219:209–220. doi:10.1016/j.jmatprotec.2014.12.025
22. Wei PS, Wu JH, Chao TC, Chen LJ (2014) Keyhole collapse during high intensity beam drilling. Int J Heat Mass Tran 79:300–308. doi:10.1016/j.ijheatmasstransfer.2014.07.070
23. Gatzen M, Thomy C, Vollertsen F (2012) Analytical investigation of the influence of the spatial laser beam intensity distribution on keyhole dynamics in laser beam welding. Laser Eng 23(1–2):109–122
24. Zhou J, Tsai HL (2007) Effects of electromagnetic force on melt flow and porosity prevention in pulsed laser keyhole welding. Int J Heat Mass Tran 50(11–12):2217–2235. doi:10.1016/j.ijheatmasstransfer.2006.10.040
25. Haboudou A, Peyre P, Vannes AB, Peix G (2003) Reduction of porosity content generated during Nd:YAG laser welding of A356 and AA5083 aluminium alloys. Mat Sci Eng a-Struct 363(1–2):40–52. doi:10.1016/S0921-5093(03)00637-3
26. El-Batahgy A, Kutsuna M (2009) Laser beam welding of AA5052, AA5083, and AA6061 aluminum alloys. Adv Mater Sci Eng . doi:10.1155/2009/974182Artn 974182
27. Lisiecki A, Burdzik R, Siwiec G, Konieczny L, Warczek J, Folega P, Oleksiak B (2015) Disk laser welding of car body zinc coated steel sheets. Arch Metall Mater 60(4):2913–2922. doi:10.1515/amm-2015-0465
28. Ahsan MRU, Kim YR, Kim CH, Kim JW, Ashiri R, Park YD (2016) Porosity formation mechanisms in cold metal transfer (CMT) gas metal arc welding (GMAW) of zinc coated steels. Sci Technol Weld Joi 21(3):209–215. doi:10.1179/1362171815y.0000000084
29. Chang B, Allen C, Blackburn J, Hilton P (2013) Thermal and fluid flow characteristics and their relationships with porosity in laser welding of AA5083. Physcs Proc 41:471–480. doi:10.1016/j.phpro.2013.03.104
30. Mohandas T, Banerjee D, Rao VVK (1999) Fusion zone microstructure and porosity in electron beam welds of an alpha plus beta titanium alloy. Metall Mater Trans A 30(3):789–798. doi:10.1007/s11661-999-0071-3
31. Gao M, Zeng XY, Hu QW, Yan J (2008) Weld microstructure and shape of laser-arc hybrid welding. Sci Technol Weld Joi 13(2):106–113. doi:10.1179/174329307x249388
32. Zhang KZ, Lei ZL, Chen YB, Liu M, Liu Y (2015) Microstructure characteristics and mechanical properties of laser-TIG hybrid welded dissimilar joints of Ti-22Al-27Nb and TA15. Opt Laser Technol 73:139–145. doi:10.1016/j.optlastec.2015.04.028